

COMPUTATIONAL FLUID DYNAMICS ANALYSIS OF A DIRECT AIR CAPTURE FILTER SYSTEM

Matthew Panagopoulos¹, Nicholas J. Lawson¹, Deanna M. D'Alessandro² & Eleanor Kearns²

¹School of Aerospace, Mechanical and Manufacturing Engineering, The University of Sydney, Camperdown, NSW 2006, Australia

²School of Chemical and Biomolecular Engineering, The University of Sydney, Camperdown, NSW 2006, Australia

Abstract

Computational Fluid Dynamics (CFD) simulations were conducted on a computational model of a Metal-Organic Framework (MOF) Direct Air Capture (DAC) filter system. Using a RANS scheme with the k- ω SST turbulence model and the SIMPLE solver, the computational model was simulated using CFD software Open-FOAM to estimate the pressure drop across the inlet and outlet of the system. Based on pipe diameter D, the pressure drop P_L was found to vary with Reynolds number, Re_D through the relationship $P_L \propto Re_D^{1.88}$. Initial results indicate the cylindrical gyroid geometry of the filter to be primarily responsible for the pressure drop, due to the formation of maximum pressure zones at regions of relative concavity.

Estimated pressure drop results were compared with experimental data for validation. A high level of agreement was observed, with the percentage error dropping below $\frac{\Delta P_L}{P_L} = 1\%$ at a Reynolds number of $Re_D = 44970$. Sources of error were analysed, with the local acceleration around the hotwire velocity probe causing an overestimation of the Reynolds number entering the cartridge. CFD was used to quantify this effect and produce a correction factor to adjust experimental results.

Keywords: Direct Air Capture, Computational Fluid Dynamics, porous absorbent, Sustainable Aviation Fuel, e-fuel

1. Introduction

Mean global temperatures have risen by an average of 0.08° C per decade since 1900, with the ten warmest years recorded since the year 1880 having all occurred since 2010 [1]. It is accepted that this increase is a result of carbon dioxide emissions originating from human activities [2]. The International Energy Agency (IEA) estimates that global energy-related emissions have been steadily increasing since the beginning of 2019, with 33 gigatonnes of carbon dioxide (C02) being released globally in 2021 [3].

Aviation is a sector which is particularly challenging to de-carbonise and to reach net-zero [4]. Small-scale electric aircraft are beginning to be produced, such as the Eviation Alice [5]. However, there are still significant challenges with weight and performance for these aircraft. This makes electrified air travel less cost effective, and hence unlikely to be viable for large scale commercial use. The use of hydrogen technologies also offers a route to net zero aviation, but these technologies are still in the initial stages of development. Further, the production of secondary CO2 emissions in conventional aircraft also contributes to operations that cannot be inherently carbon neutral. Two approaches that are seen as options for aviation to reach net-zero, as a part of a series of measures, are to transition to Sustainable Aviation Fuel (SAF) [6] and to apply carbon capture and removal technologies [7]. It is likely a combination of these two technologies is required. Removal of carbon dioxide from the atmosphere through Direct Air Capture (DAC) technologies would bring aviation closer to carbon neutrality by effectively offsetting unavoidable emissions. In the former case, carbon removal can also be used to provide carbon dioxide feedstock for the fuel in electro-fuel (e-fuel) production processes [8][9].

A DAC device is in development at The University of Sydney's Net Zero Institute (NZI), in partner-ship with Southern Green Gas and AspiraDAC, to remove carbon dioxide from the atmosphere [10]. The device is scalable, solar powered, and easily manufacturable. With this device, unavoidable emissions can be removed from the atmosphere and sequestered underground, or repurposed as a feedstock for e-fuel production. As presented in Figure 1, a number of cartridges are contained within the DAC device. Each cartridge comprises of a canister housing a 3D cylindrical gyroid filter made from a Metal-Organic Framework (MOF). MOF's are a class of compounds consisting of metal ions coordinated to organics to form three-dimensional structures [11]. MOF's filters are highly porous, capable of soaking up large amounts of a specific gas molecule. The filter of this cartridge system has been designed to have a porosity such that it captures carbon dioxide from the air. The filter is hence cycled between capturing carbon dioxide, and being expanded through heat such that it releases the carbon dioxide from its pores.



Figure 1 – DAC Device [10]

The objectives of the present paper are to assess the validity of the Computational Fluid Dynamics (CFD) simulations of a computational model of the DAC filter system through comparison with experimental pressure drop data. The performance of the DAC filter system will hence be assessed by analysing the source of the pressure drop across the canister and its dependence on Reynolds number (Re_D). Numerical methods will account for and explain differences between computational predictions and experimental results.

2. Literature Review

2.1 CFD Techniques for Modelling Filter Systems

CFD is used to model the flow through number of types of filter systems, including water treatment systems [12], and computer CPU cooling [13]. Reynolds Averaged Navier Stokes (RANS) simulation schemes are often used in these studies [14][15], giving a time-averaged solution in a context where instantaneous fluctuations in the fluid flow state are irrelevant [16]. In [17], a RANS scheme is used with the Semi-Implicit Method for Pressure Linked Equations (SIMPLE) numerical solver [18] to investigate the flow properties through a carbon cloth used for Volatile Organic Compounds (VOC) treatment, where CFD analysis is conducted on a cylindrical canister with a porous filter placed inside at its midpoint. The SIMPLE algorithm is commonly used in this context [19], and is found to be effective in providing more efficient and robust single phase flows [20].

Computational models for filter systems are validated by comparing the results to experimental data [17][19][21][14]. CFD results are replicated by experiment, and agreement is assessed by comparing predicted values of a certain defined quantity. Satisfactory agreement between the computational results and experiment was reached in [17] with a maximum difference of 28% between predicted and measured pressure drop, with similarities observed in other cited papers. Similar metrics will be used in the present paper.

ANSYS Fluent is predominantly used in the application of CFD to simulate the flow through a filter system [19][21][14]. Other CFD software, such as OpenFOAM, were rarely used in place of ANSYS for these applications. However, OpenFOAM is open source with extensive user documentation and

tutorials produced by the provider. This makes OpenFOAM well equipped to evolve the computational model of the filter in future studies, when variables such as heat transfer are included.

2.2 Turbulence Modelling

When using the RANS equations, turbulence models are used to ensure the six additional flow stress terms that appear in the momentum equation are closed in what is called the closure method [16]. Turbulence and boundary layer effects will have a significant contribution to pressure drop values across a filter in reality, so turbulence models are very often used in this context.

The standard k- ε turbulence model has been used extensively in the context of numerically simulating the flow through a filter system [19][17][15]. In the closure method used with the RANS approximated Navier-Stokes equations, the turbulent kinetic energy k is calculated using Equation 1. The dissipation rate of the turbulent kinetic energy ε , dominated by work performed by the fluctuations of viscous stresses [22], can be estimated using Equation 2 [23]. Within the k- ε turbulence model, the coefficient for the turbulent viscosity is taken as $C_{\mu}=0.09$ [24]. It has been found that poor performance is typically exhibited in simulating flow over curved boundary layers [25], a flow feature that will be important in estimating the effect of the complex filter geometry.

$$k = \frac{3}{2} (I \cdot v_{avg})^2 \tag{1}$$

$$\varepsilon = \frac{C_{\mu}^{0.75} k^{1.5}}{L_T} = \frac{0.09^{0.75} k^{1.5}}{L_T} \tag{2}$$

The standard k- ω turbulence model estimates the turbulent kinetic energy, and the specific dissipation rate ω using Equation 3, with the coefficient for the turbulent viscosity taken as $C_{\mu}=0.09$. The k- ω turbulence model is most useful in simulating near-wall boundary layer flows, although is not as effective in simulating free shear flows like the k- ε model [26]. The k- ω SST turbulence model is used more commonly in the CFD simulation of filter systems [21]. The model combines the near-wall boundary layer efficiencies of the standard k- ω model, and the free shear simulating abilities of the k- ε model. The application of the k- ω SST turbulence model in filter simulation is not well reported, and further research is required [27].

$$\omega = \frac{k^{0.5}}{C_u^{0.25} \cdot L_T} = \frac{k^{0.5}}{0.09^{0.25} \cdot L_T}$$
 (3)

3. CFD

OpenFOAM v10 was chosen as the CFD software to simulate the flow properties of the cartridge system. For the scope of this project, OpenFOAM's simpleFoam solver was considered to be an appropriate choice of numerical solver, taking velocity and pressure boundary conditions, as well as the wall function boundary conditions corresponding to the chosen turbulence model. The simpleFoam solver uses the SIMPLE algorithm [18] to solve the continuity condition and momentum equation given in Equation 4 and Equation 5 respectively.

$$\nabla \cdot \mathbf{u} = 0 \tag{4}$$

$$\nabla \cdot (\mathbf{u} \otimes \mathbf{u}) - \nabla \cdot \mathbf{R} = -\nabla p + \mathbf{S}_{\mathbf{u}} \tag{5}$$

This section outlines the steps involved in simulating and predicting the pressure drop across the computation model of the DAC filter using CFD. The construction of the computational model and convergence study results are described, and the choice of turbulence model is discussed. Obtained pressure drop predictions are then presented and discussed.

3.1 Description of Geometry and Configuration

The simulated system consists of a cylindrical gyroid filter, housed within a canister. The canister is made up of a cylindrical capture chamber, with inlet and outlet sections of a smaller radius. The dimensions of the canister and the housed filter, as they are defined in the CFD case setup, have been summarised in Table 1.

Dimension	Value (mm)
Inlet Section Diameter	35
Inlet Section Length	20
Capture Chamber Diameter	60
Capture Chamber Length	85.7
Outlet Section Diameter	35
Outlet Section Length	600
Filter Diameter	60
Filter Length	74.8

Table 1 – Dimensions of Computational Model

The static pressure measurement points are defined in the inlet and outlet sections 10 mm either side of the capture chamber. Static pressure measurements were taken using OpenFOAM's integration tool. The kinematic pressure was integrated over the inlet/outlet pipe cross-section at the measurement points to obtain an average value, which were then converted to a static pressure. A cross-section of the CFD domain of the canister is shown in Figure 2. The outlet section had been made longer than the inlet section by a length of approximately $10D_{capture}$ to produce a developed flow at the outlet of the canister, ensuring accurate results at the outlet static pressure measurement point.

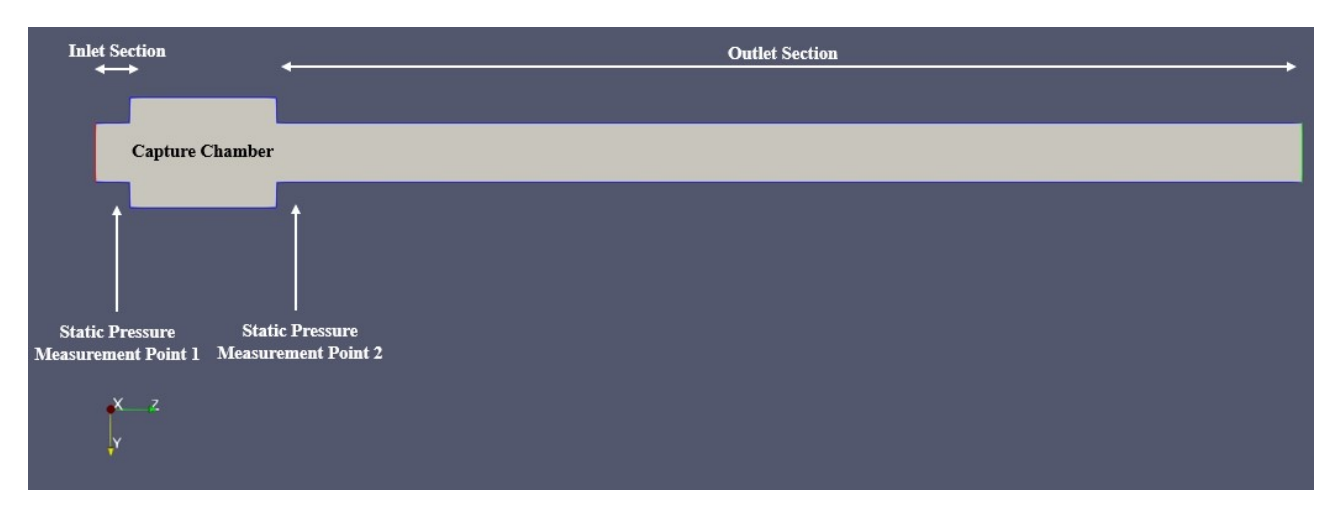


Figure 2 – Cross-Section of CFD Model of Canister

The filter is placed within the capture chamber of the canister, equidistant from the inlet and outlet sections. An image of the filter inserted within the canister is given in Figure 3a. A cross-section of the complete cartridge system is shown in Figure 3b.

3.2 Convergence Study

Convergence testing was conducted for four test cases. The test cases, and their corresponding mesh distribution, are summarised in Table 2.

Convergence testing was conducted by predicting the static pressure drop corresponding to a Reynolds number of $Re_D=18740$. The Reynolds number corresponding to flow through the canister is determined using the weighted average diameter between the static pressure measurement points D_{avg} , and the average velocity derived from the mass flow rate v_{avg} . The Reynolds number of flow through the canister is hence formulated using Equation 6.

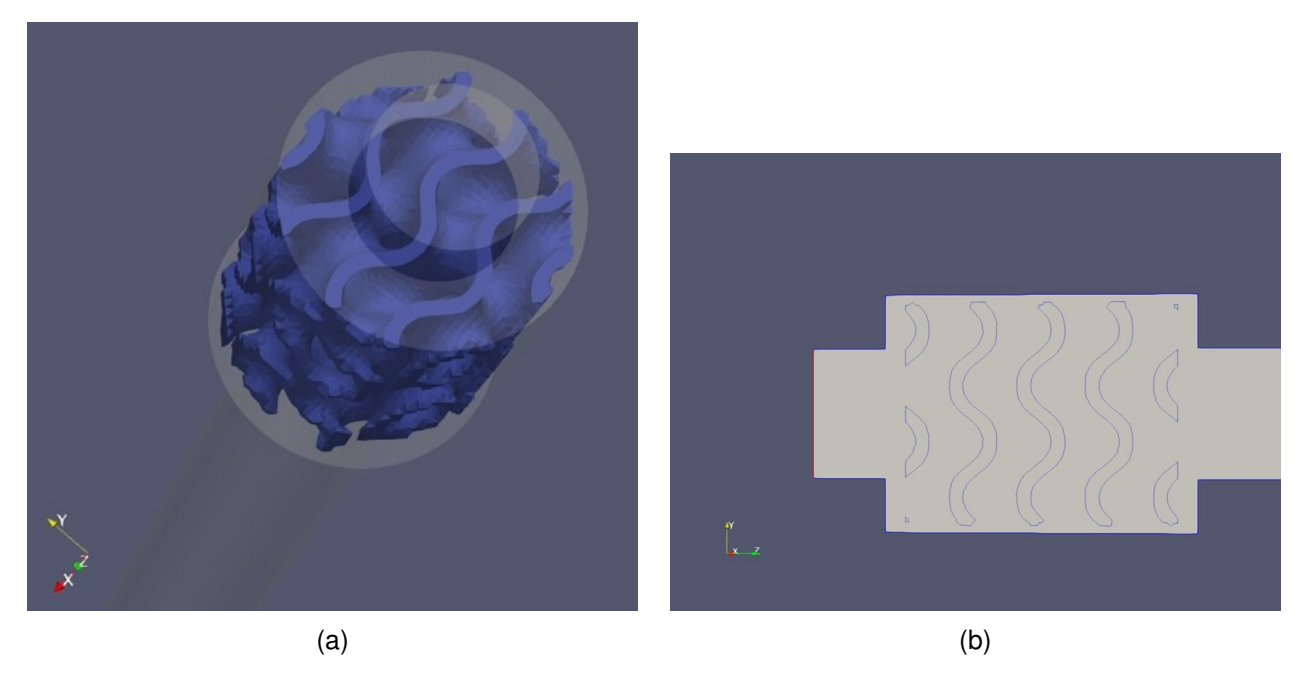


Figure 3 – Filter in Capture Chamber of Canister (a). Cross Section of System (b)

Number of Cells Before Filter Insertion						
Mesh Parameter	Case 1	Case 2	Case 3	Case 4		
Inlet Section	39858	139776	219558	318864		
Outlet Section	39858	139776	219558	318864		
Capture Chamber	526680	1820160	2867130	4213440		
Total	606396	2099712	3306246	4851168		
Number of Cells After Filter Insertion						
Mesh Parameter	Case 1	Case 2	Case 3	Case 4		
Total	1309216	1667616	2626697	3854524		

Table 2 – Tested Cell Counts for Convergence Test Cases

$$Re_{D} = \frac{\rho v_{avg} D_{avg}}{\mu} = v_{inlet} \left(\frac{D_{inlet}}{D_{avg}}\right)^{2} \frac{\rho D_{avg}}{\mu}$$
 (6)

The convergence results for the pressure drop across the canister are shown in Figure 4.

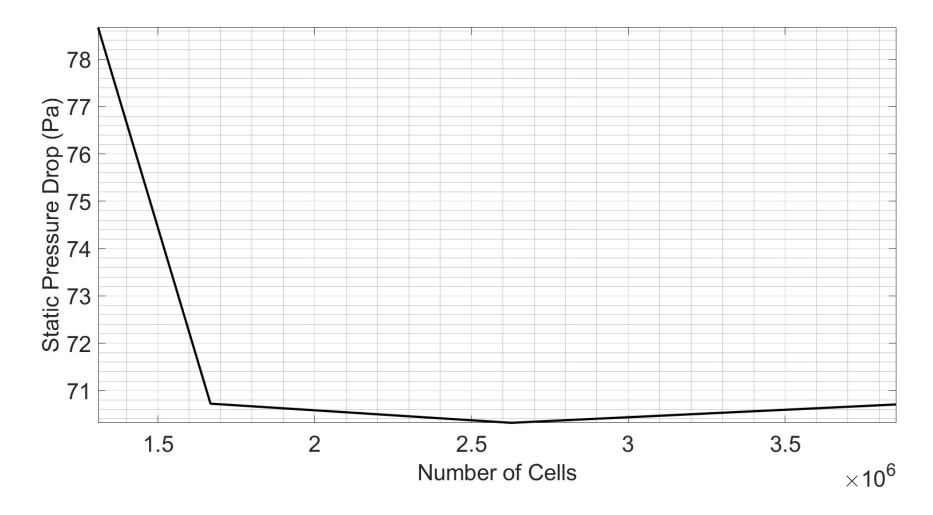


Figure 4 – Static Pressure Drop vs. Cell Count ($Re_D = 18740$)

Results show that the cell density's used in test case 3 and 4 provide predictions approaching mesh independence. The Grid Convergence Index (CGI) of the tested mesh's are calculated using Equation 7. Equation 7 assumes a safety factor of $F_s = 1.25$, a value often used for comparisons over multiple mesh densities [28]. A numerical scheme of second order is used, hence defining the order of convergence as p = 2.

$$CGI = \frac{F_s|\Omega|}{r^p - 1} = \frac{1.25}{r^2 - 1} \left| \frac{P_{L_1} - P_{L_2}}{P_{L_1}} \right|$$
 (7)

The CGI values of test case 3 and 4 are summarised in Table 3. Test case 3 has a lower CGI value and requires less computation time to provide converged predictions, and hence was used throughout the present study.

Test Case i	$r = \frac{n_i}{n_{i-1}}$	$ \Omega $	CGI
Test Case 3	1.575	0.0058	0.4856%
Test Case 4	1.467	0.0055	0.5944%

Table 3 - Convergence Study CGI Results

3.3 Numerical Models

The RANS time-averaged equations are used in the simulations as the time-averaged pressure drop is of interest rather than its instantaneous fluctuations.

For a Reynolds number of $Re_D=3748$, the maximum non-dimensional wall unit value throughout the canister is $y^+=1.087$ in the inlet section. In the capture chamber, this reduces to $y^+=0.2561$. At the highest simulated Reynolds number of $Re_D=51340$, the y^+ values are greater, reaching $y^+=10.07$ in the inlet section and $y^+=2.417$ in the capture chamber. These measured y^+ values indicate the necessity of turbulence model wall functions to describe the flow features inside the capture chamber accurately. The literature review identified two types of turbulence models that are commonly used in the simulation of filter systems under an RANS numerical scheme; the k- ε turbulence model, and the k- ω SST turbulence model. These two turbulence models were used to simulate the flow through the canister for a Reynolds number of $Re_D=18740$.

Turbulence Model	Static Pressure Drop (Pa)
k-ε	69.10
$k-\omega$ SST	70.72

Table 4 – Pressure Drop for Predicted by Turbulence Models ($Re_D = 18740$)

Without a significant difference between the results predicted by the two selected turbulence models, the RANS $k-\omega$ SST model was used throughout this study with the appropriate wall functions. The $k-\omega$ SST model provides the best description of near-wall boundary layer effects while maintaining the free shear simulating advantages of the $k-\varepsilon$ model. Further, the $k-\varepsilon$ model typically exhibits poor performance in simulating flow over curved boundary layers, something which will be especially prominent in the filter region of the capture chamber.

3.4 Results

The pressure drop across the complete cartridge system was estimated for the range of Reynolds numbers from $Re_D = 3748$ to $Re_D = 51340$ using CFD. The static pressure drop results across the complete cartridge system are shown in Figure 5.

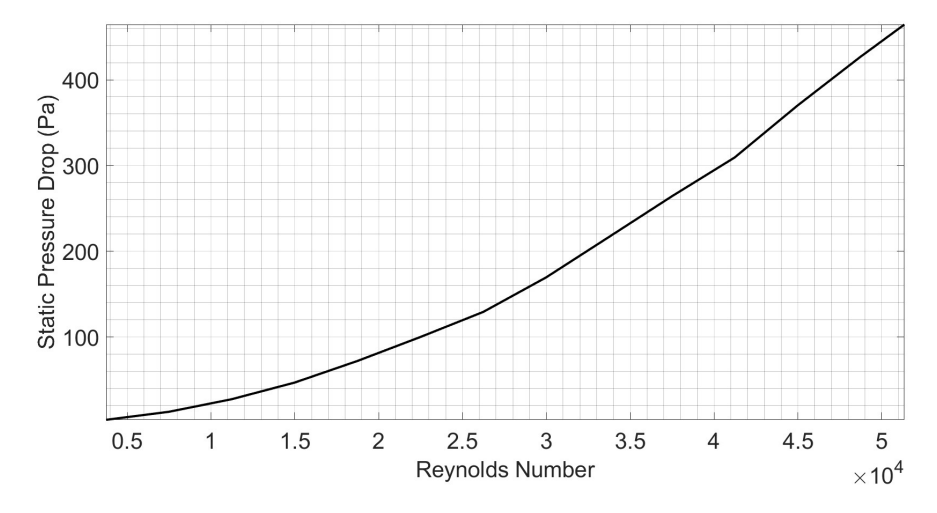


Figure 5 – Predicted Pressure Drop

The static pressure drop across the system increases from $P_L = 3.3 \text{Pa}$ at a Reynolds number of $Re_D = 3748$ to $P_L = 464.5 \text{Pa}$ at a Reynolds number of $Re_D = 51348$. The pressure drop across the system increases with the relationship $P_L \propto Re_D^{1.88}$. Observing the velocity profile of the simulation, it becomes apparent that this pressure loss is resultant of the interaction between the flow of different regions in the filter. When the flow is passing through the gyroid geometry, it will encounter either a region of relative convexity, or a region of relative concavity. A region of relative convexity is, from the perspective of the oncoming flow, a region of peak suction, whereas a region of relative concavity is a region of peak pressure. The pressure losses experienced with the inclusion of the filter occur due to the introduction of high pressure zones in the regions of relative concavity. Figure 6 shows the pressure profile of the canister and filter system at a Reynolds number of $Re_D = 26230$.

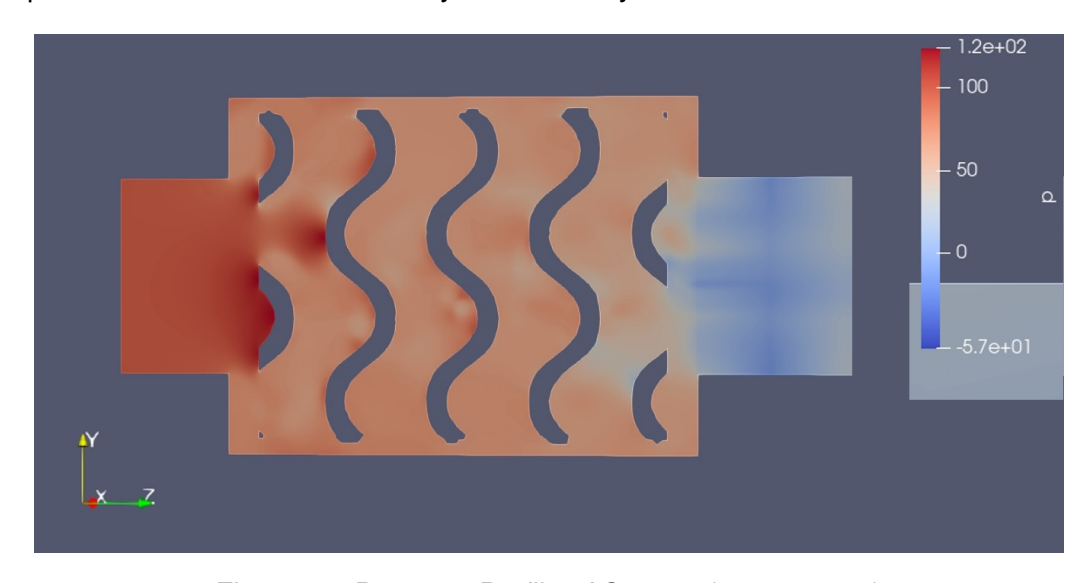


Figure 6 – Pressure Profile of System ($Re_D = 26230$)

Figure 6 shows that the regions of relative concavity have a greater average pressure than those of relative convexity. The CFD simulations have shown that when the flow approaches a region of relative concavity, it effectively gets trapped with nowhere else to go. This creates a high pressure region, as the local fluid density has been increased by the accumulation of air. As new flow approaches the high pressure regions that have formed, the fluid is subject to an adverse pressure gradient. Incoming flow is hence convected towards the regions of peak suction when approaching regions of relative concavity. This results in separation of the flow, and the generation of vortices.

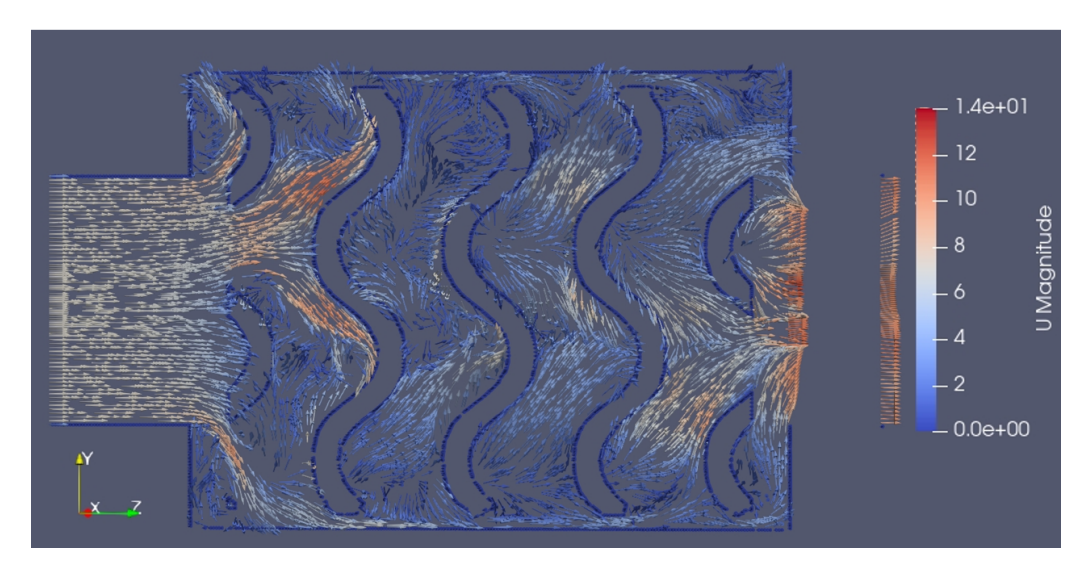


Figure 7 – Velocity Profile of System ($Re_D = 26230$)

The fact that turbulent flow is facilitated by the gyroid geometry in regions of high suction is illustrated by the velocity profile shown in Figure 7. In the regions of relative concavity there is no uniform direction to the velocity of the flow, hence giving a high level of turbulent kinetic energy. Figure 8 plots the turbulent kinetic energy along lines of relative concavity and convexity across the gyroid at a Reynolds number of $Re_D = 26230$.

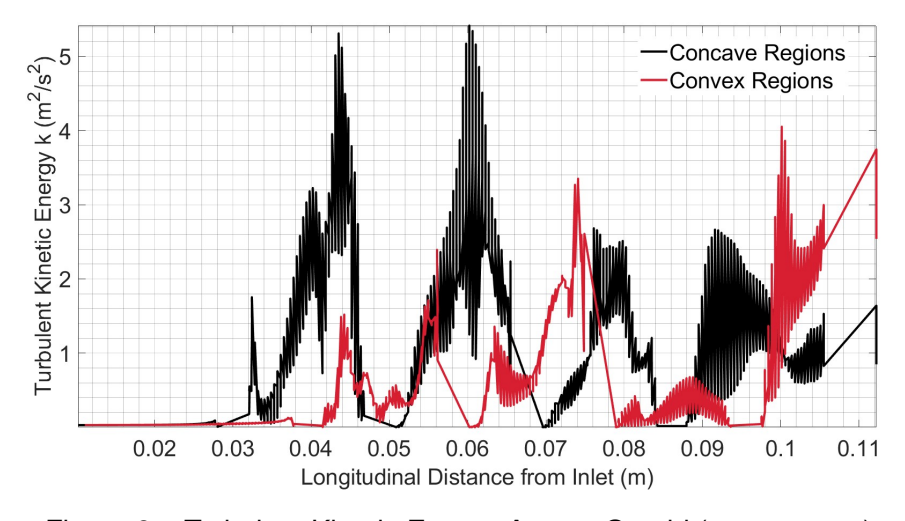


Figure 8 – Turbulent Kinetic Energy Across Gyroid ($Re_D = 26230$)

It is clearly shown in Figure 8 that the turbulent kinetic energy in concave regions of the filter is significantly greater than in convex regions. In flow with a high level of turbulent kinetic energy, there is a greater rate of energy dissipation. The energy losses associated with the formation of high pressure regions throughout the filter are hence directly responsible for the large static pressure drops predicted. A greater Reynolds number will produce stronger regions of suction due to a greater adverse pressure gradient faced by oncoming flow, and hence turbulence in these areas will be increased. It is sensible that this would cause a greater pressure drop across the filter, as observed in Figure 5.

4. Experiment

The computational model was validated by comparing the predicted static pressure drop with experimentally obtained data. The relationship between Reynolds number and the static pressure drop across the cartridge can be found experimentally without too much difficulty. The CFD model is considered valid if the computational predictions and experimental results are in agreement. If the

computational model is found to be valid, other flow properties that are difficult to experimentally obtain can be taken from the simulation with greater confidence that they are accurate.

This section outlines each step that was taken in order to ensure an experiment was conducted with reproducible outcomes. The atmospheric conditions on the day of testing are presented. The apparatus required, the construction of the experiment, and the experimental methodologies used are explained in detail. The results are then analysed, with particular focus on any difference found between the computationally obtained results. Reasons as to why these differences may exist, and steps taken to account for these differences, will be a focus.

4.1 Experimental Setup and Apparatus

The setup of this experiment consisted of a fan to drive airflow, leading to a length of PVC piping ending in a valve that regulated the mass flow rate. Downstream of the valve was another length of piping with a hotwire velocity probe inserted. The canister system containing the gyroid filter was then attached with static pressure measuring equipment in the inlet and outlet sections.

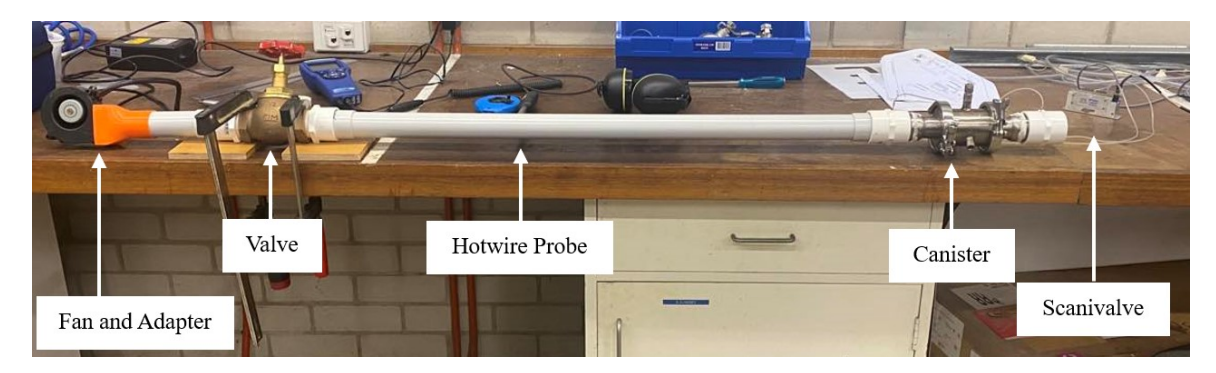


Figure 9 - Experimental Setup

The airflow in this experiment was driven by a Blower San Ace B97 provided by Sanyo Denki [29]. The fan was operated using a 12V DC supply rated at 6.2A. The outlet duct has dimensions of 60mm in height, and 33mm in width. The fan was measured to provide a base mass flow rate of $\dot{m} = 0.01607 \text{kg/s}$.

The airflow driven by the fan was directed into the rest of the experimental setup through the use of a custom 3D printed adapter. The outlet of the adapter had a diameter of 38mm. 150mm of 38mm diameter PVC piping was hence used to connect the fan to a valve. A CIM 75-09 $1\frac{1}{2}$ in Globe Valve by Cimberio Valve Technological Solutions was used in this experiment [30]. This valve design is typical for applications in which fine flow regulation is required.

850mm of 38mm diameter PVC piping was used to connect the globe valve to the filter system. Velocity measurements were taken 600mm upstream of the canister using a VelociCalc Air Velocity Meter Model 9565 Series hotwire probe. The hotwire probe was inserted into the PVC piping and was secured in place using electrical tape. The hotwire probe used in this experiment measures the heat transfer by maintaining constant wire temperature through a feedback system, making the voltage across the wire proportional to velocity [31]. The probe was operated using mains power with the provided AC adapter.

Two pressure ports were used to take measurements; one 10mm from the inlet of the capture chamber, one 10mm from the outlet of the capture chamber. The pressure taps were connected to a Scanivalve MPS 4264 to record pressure measurements. Data was recorded by the Scanivalve over a 30s period at a sampling frequency of 200Hz. Experimental static pressure data used in calculations and presentation of this report will use the mean of the pressure measurements taken over the sampling period.

4.2 Methodology

After constructing the experiment, the Scanivalve was connected to the data acquisition software, which was run through MatLab. Atmospheric conditions were then recorded.

The valve was initially opened completely in order to measure the maximum flow velocity recorded by the probe. It was found that the maximum flow velocity produced by the fan was 13.7m/s. The flow conditions to be tested in the experiment were hence defined.

With the valve still completely open and the hotwire probe reading stable velocity values, the Scanivalve data acquisition software began recording over the specified period of 30s. The data from the Scanivalve and hotwire probe was saved locally. The valve was then adjusted to repeat the static pressure measurements for each Reynolds number.

4.3 Instrument Error

The accuracy of the instruments used in this experiment are summarised to understand the uncertainties in the obtained results.

4.3.1 Hotwire Probe

The hotwire probe was used to measure the ambient temperature and velocity of the flow. The accuracy of the instrument in the measuring of these quantities is:

- Velocity $\pm 3\%$ of reading, with a resolution of 0.01m/s, and a response time of 200ms
- Temperature $\pm 0.3^{\circ}$ C, with a resolution of 0.1° C, and a response time of 2min (to 66% of final value)

4.3.2 Scanivalve

The Scanivalve was used to measure the static pressure at the inlet and outlet of the cartridge. The Scanivalve has an accuracy of $\pm 0.06\%$ of the reading at around atmospheric pressure.

4.4 Experimental Error

What must be considered before the computational model is validated is whether the hotwire probe is accurate in it's measurement of the local flow velocity in the pipe. As the flow encounters the hotwire probe, due to the probe dimensions, and through flow continuity and conservation of mass, the oncoming flow will be accelerated around the probe region, before returning to normal freestream conditions, downstream of the probe. The hotwire probe hence measures a locally accelerated flow, not the flow conditions entering the cartridge.

CFD simulations were conducted to quantify the effect of the local acceleration on the flow velocity measured by the hotwire probe. It was found that the local acceleration effects were substantial, causing a 136% overestimation of the flow velocity at a Reynolds number of $Re_D=2577$, and a 115% overestimation of the flow velocity at a Reynolds number of $Re_D=35300$. A correction factor polynomial was derived using the results from the hotwire CFD simulations. This correction factor, when applied to the experimentally measured Reynolds number, corrected for the local acceleration effects. This work will be the subject of a further paper.

4.5 Results

The results from the experiment are plotted together with the computational predictions in Figure 10. Figure 10 shows that there is a high level of agreement between the computational predictions and experimental results. The computationally predicted values for the static pressure drop across the cartridge consistently align with the experimental values within their given errors. Figure 11 shows the error in the CFD predictions as a percentage of the experimental pressure drop data.

The percentage error decreases from $\frac{\Delta P_L}{P_L} \approx 33\%$ at a Reynolds number of $Re_D=3195$, to $\frac{\Delta P_L}{P_L} \approx 0.54\%$ at a Reynolds number of $Re_D=51720$. It is shown that there is an overall high level of agreement between the experimental results and CFD predictions. Despite a high percentage error at the lower Reynolds numbers tested, the CFD predictions are well within one standard deviation of the experimental results. Higher Reynolds numbers have a significantly lower percentage error. Overall, all results lie within the standard 95% confidence interval, confirming the validity of the CFD to model the DAC cartridge system.

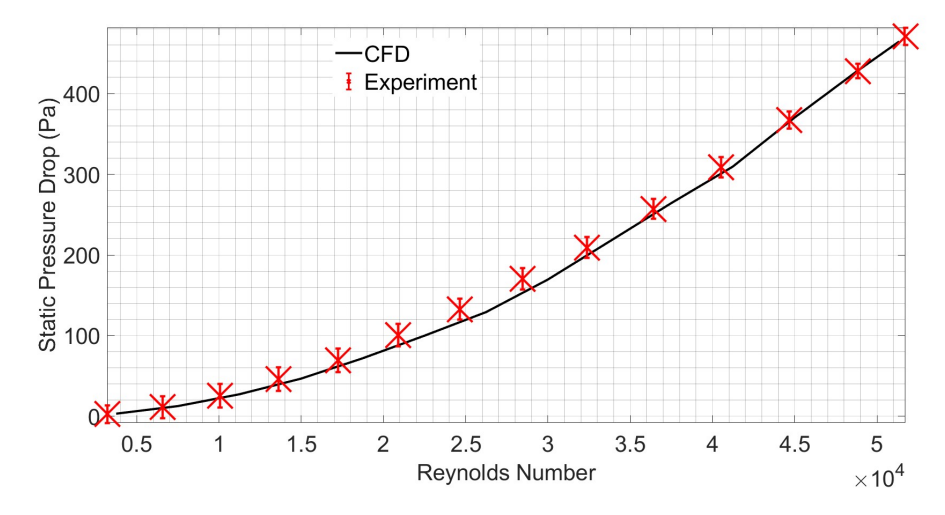


Figure 10 – Experimental Results and Computational Predictions

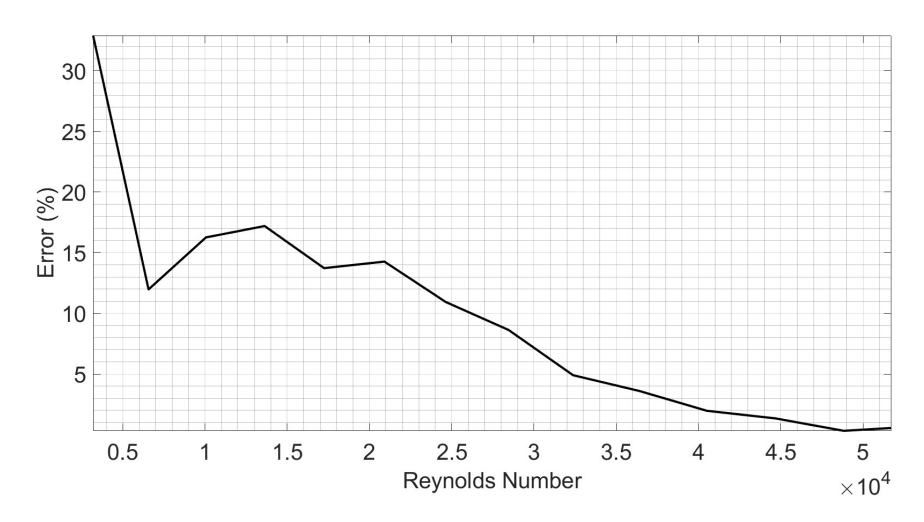


Figure 11 – CFD Error Percentage of Experimental Value

5. Conclusion

This paper has presented a CFD model to predict the static pressure drop across the cartridge of a DAC device. A canister housing a cylindrical gyroid filter was modelled computationally in OpenFOAM and the CFD solutions compared the experimental pressure drop results from a printed filter and DAC filter holder.

The flow through the scaled down computational model of the cartridge system was simulated for a number of Reynolds numbers. The obtained results gave the estimated pressure drop P_L across the system, in the form $P_L \propto Re_D^{1.88}$, where Re_D is Reynolds number based on pipe diameter. Analysis found that pressure losses were associated with an increase in turbulent kinetic energy produced in the filter regions of peak pressure.

The experiment measured the static pressure drop at the inlet and outlet of the cartridge. There was a high level of agreement between the computational predictions and experimental results. The percentage error of the CFD predictions were greater in the low Reynolds number regimes, but still within one standard deviation of experiment. The CFD predictions were more accurate in the high Reynolds number regimes, with the percentage error dropping below $\frac{\Delta P_L}{P_L} = 1\%$ at $Re_D = 44970$.

The primary source of error between the computational predictions and experimental results was identified to be the local acceleration around the hotwire probe. The physical pressure of the probe accelerated the local flow in the pipe, overestimating the Reynolds number at the inlet of the cartridge. CFD simulations were conducted to quantify the local acceleration around the hotwire of the velocity probe. Results indicated that the local acceleration was not constant with the flow regime, and needed

to be treated as being dependent on the measured velocity. The results obtained from the hotwire probe CFD simulations enabled the formulation of a variable correction factor, applied to experimental results to reflect the accurate flow conditions leading into the filter system. This is the subject of a further paper.

Overall, the findings of this paper have shown that the CFD model of the DAC cartridge system is valid in predicting the static pressure drop, to within experimental error. Further work will now focus on more experimental work to map the detailed flow inside the filter.

References

- [1] R. LINDSEY and L. DAHLMAN, "Climate change: Global temperature," *National Oceanic and Atmospheric Administration*, Jan. 2023.
- [2] Intergovernmental Panel on Climate Change (IPCC), Climate Change 2021 The Physical Science Basis: Working Group I Contribution to the Sixth Assessment Report of the Intergovernmental Panel on Climate Change. Cambridge University Press, 2023. DOI: 10.1017/9781009157896.
- [3] IEA, "Net zero by 2050," IEA, 2021.
- [4] T. H. Karakoc, R. Das, I. Ekmekci, A. Dalkiran, and A. H. Ercan, *Approaches in Sustainable Aviation Proceedings of International Symposium on Sustainable Aviation*. Springer Nature Switzerland, 2024. DOI: 10.1007/978-3-031-33118-3.
- [5] N. Ahituv, "Air travel is destroying the planet. an israeli-developed electric plane is one solution," *HAARETZ*, Aug. 2023.
- [6] International Civil Aviation Organization (ICAO), *Sustainable Aviation Fuels Guide*. United Nations, 2018.
- [7] IEA, "Direct air capture 2022," IEA, 2022.
- [8] R. H. Williams, *Fuel decarbonization for fuel cell applications and sequestration of the sepa-rated CO2*. Centre for Energy and Environmental Studies, Princeton University, 1996.
- [9] I. S. Petter Krus and A. A. Oliveira, "Hybrid electric propulsion system optimization for a commuter aircraft," Sep. 2022.
- [10] S. G. Gas, *Our technology*, Available at https://www.southerngreengas.com.au/our-technology/.
- [11] S. R. Batten, N. R. Champness, X.-M. Chen, et al., Pure and Applied Chemistry, vol. 85, no. 8, pp. 1715–1724, 2013. DOI: doi:10.1351/PAC-REC-12-11-20. [Online]. Available: https://doi.org/10.1351/PAC-REC-12-11-20.
- [12] A. Afkhami, A. Brown, L. P. Sabogal-Paz, D. Dixon, N. G. Ternan, and P. S. Dunlop, "A comprehensive approach to simulation of cartridge filtration using cfd," *Journal of Environmental Chemical Engineering*, vol. 11, no. 5, 2023. DOI: 10.1016/j.jece.2023.110756. [Online]. Available: https://www.scopus.com/inward/record.uri?eid=2-s2.0-85170555900&doi=10.1016%2fj.jece.2023.110756&partnerID=40&md5=997d0286f2e1a34dda60bda3b0f118d7.
- [13] V. S. Simon, L. S. Reddy, P. Shahi, et al., "Cfd analysis of heat capture ratio in a hybrid cooled server," 2022. DOI: 10.1115/IPACK2022-97445. [Online]. Available: https://www.scopus.com/inward/record.uri?eid=2-s2.0-85144620015&doi=10.1115%2fIPACK2022-97445&partnerID=40&md5=fac4eb5a3029ff90540220a560230d40.
- [14] J.-N. Baléo and A. Subrenat, Pierre Le Cloirec, "Numerical simulation of flows in air treatment devices using activated carbon cloths filters," *Chemical Engineering Science*, vol. 55, no. 10, pp. 1807—1816, 2000, ISSN: 0009-2509. DOI: https://doi.org/10.1016/S0009-2509(99)00441-8. [Online]. Available: https://www.sciencedirect.com/science/article/pii/S0009250999004418.

- [15] E. Ryan, D. DeCroix, R. Breault, et al., "Multi-phase cfd modeling of solid sorbent carbon capture system," Powder Technology, vol. 242, pp. 117–134, 2013, Selected Papers from the 2010 NETL Multiphase Flow Workshop, ISSN: 0032-5910. DOI: https://doi.org/10.1016/j.powtec.2013.01.009. [Online]. Available: https://www.sciencedirect.com/science/article/pii/S0032591013000260.
- [16] N. A. Che Sidik, S. N. A. Yusof, Y. Asako, S. Mohamed, and A. Aziz, "A short review on rans turbulence models," *CFD Letters*, vol. 12, pp. 83–96, Nov. 2020. DOI: 10.37934/cfdl.12.11.8396.
- [17] A. Subrenat, J. Bellettre, and P. Le Cloirec, "3-d numerical simulations of flows in a cylindrical pleated filter packed with activated carbon cloth," *Chemical Engineering Science*, vol. 58, no. 22, pp. 4965–4973, 2003, ISSN: 0009-2509. DOI: https://doi.org/10.1016/j.ces.2003.07.012. [Online]. Available: https://www.sciencedirect.com/science/article/pii/S0009250903003580.
- [18] L. S. Caretto, A. D. Gosman, S. V. Patankar, and D. B. Spalding, "Two calculation procedures for steady, three-dimensional flows with recirculation," in *Proceedings of the Third International Conference on Numerical Methods in Fluid Mechanics*, H. Cabannes and R. Temam, Eds., Berlin, Heidelberg: Springer Berlin Heidelberg, 1973, pp. 60–68, ISBN: 978-3-540-38392-5.
- [19] J. Lopes, J. Silva, S. Teixeira, and J. Teixeira, "Numerical modeling and optimization of an air handling unit," *Energies*, vol. 14, no. 1, 2021. DOI: 10.3390/en14010068. [Online]. Available: https://www.scopus.com/inward/record.uri?eid=2-s2.0-85106199290&doi=10.3390%2fen14010068&partnerID=40&md5=9ced53fa86db69d58a46c31420ee8499.
- [20] J. H. Ferziger and M. Perić, *Computational Methods for Fluid Dynamics*, 3rd ed. Springer Berlin, Heidelberg, 2012.
- [21] M. Sedlář, T. Krátký, and J. Langer, "Numerical and experimental investigation of three-dimensional flow in combined protective canister filters," *Fluids*, vol. 7, no. 5, 2022, ISSN: 2311-5521. DOI: 10.3390/fluids7050171. [Online]. Available: https://www.mdpi.com/2311-5521/7/5/171.
- [22] J. Cousteix, "Aircraft aerodynamic boundary layers," in Encyclopedia of Physical Science and Technology (Third Edition), R. A. Meyers, Ed., Third Edition, New York: Academic Press, 2003, pp. 301–317, ISBN: 978-0-12-227410-7. DOI: https://doi.org/10.1016/B0-12-227410-5/00906-6. [Online]. Available: https://www.sciencedirect.com/science/article/pii/B0122274105009066.
- [23] G. Wang, F. Yang, K. Wu, et al., "Estimation of the dissipation rate of turbulent kinetic energy: A review," Chemical Engineering Science, vol. 229, p. 116133, 2021, ISSN: 0009-2509. DOI: https://doi.org/10.1016/j.ces.2020.116133. [Online]. Available: https://www.sciencedirect.com/science/article/pii/S0009250920306655.
- [24] B. Launder and D. Spalding, "The numerical computation of turbulent flows," *Computer Methods in Applied Mechanics and Engineering*, vol. 3, no. 2, pp. 269–289, 1974, ISSN: 0045-7825. DOI: https://doi.org/10.1016/0045-7825(74)90029-2. [Online]. Available: https://www.sciencedirect.com/science/article/pii/0045782574900292.
- [25] I. A. S. Larsson, E. M. Lindmark, T. S. Lundström, and G. J. Nathan, "Secondary flow in semi-circular ducts," *Journal of Fluids Engineering*, vol. 133, no. 10, p. 101206, Oct. 2011, ISSN: 0098-2202. DOI: 10.1115/1.4004991. eprint: https://asmedigitalcollection.asme.org/fluidsengineering/article-pdf/133/10/101206/5650124/101206_1.pdf. [Online]. Available: https://doi.org/10.1115/1.4004991.
- [26] D. C. Wilcox, "Formulation of the k-w turbulence model revisited," *AIAA Journal*, vol. 46, no. 11, pp. 2823–2838, 2008. DOI: 10.2514/1.36541. eprint: https://doi.org/10.2514/1.36541. [Online]. Available: https://doi.org/10.2514/1.36541.
- [27] F. Menter, M. Kuntz, and R. Langtry, "Ten years of industrial experience with the sst turbulence model," *Heat and Mass Transfer*, vol. 4, Jan. 2003.

- [28] J. Slater, *Examining spatial grid convergence*, Available at https://www.grc.nasa.gov/www/wind/valid/tutorial/spatconv.html (2021/10/02).
- [29] San ace cooling systems fan instruction manual, 3rd ed., P/N 9BMC12P2G001, Sanyo Denki Co. LTD, 3-33-1 Minami-Otsuka, Toshima-ku, Tokyo, 2021.
- [30] Valve guide, p. 46, Cimberio Valve Technological Solutions, 2010.
- [31] Velocicalc air velocity meter model 9565 series operation and service manual, P/N 6004851, Revision G, TSI Incorperated, Mar. 2022.